# Study on fabrications and electrochemical performance of $Fe_9S_{10}$@C composite materials

Jianke Li [a,c], Guiying Xu [a], Xincheng Miao [a,c,*], Beibei Han [b,e], Kunkui Wu [a,**], Kun Wang [a,d], , Baigang An [a], Dongying Ju [b,f], Maorong Chai [b], Weimin Zhou [a,**]

[a] Key Laboratory of Energy Materials and Electrochemistry Research Liaoning Province, University of Science and Technology Liaoning, No. 189, Qianshan Middle Road, Lishan District, Anshan City, Liaoning Province 114051, China
[b] Advanced Science Research Laboratory, Saitama Institute of Technology, 1690, Fusaiji, Fukaya, Japan
[c] School of Materials and Metallurgy, University of Science and Technology Liaoning, No. 189, Qianshan Middle Road, Lishan District, Anshan City, Liaoning Province 114051, China
[d] Sinosteel Anshan Research Institute of Thermo-Energy Co., Ltd., No. 301 Anqian Road, High-tech Zone, Anshan City, Liaoning Province 114051, China
[e] Key Laboratory of Advanced Fuel Cells and Electrolyzers Technology of Zhejiang Province, Ningbo Institute of Materials Technology and Engineering, Chinese Academy of Sciences, Ningbo, No. 1219 Zhongguan West Road, Zhejiang 315201, China
[f] Hainan University, 58 Renmin Avenue, Haikou 570228, China

## ARTICLE INFO

## ABSTRACT

The low-cost preparation of $Fe_9S_{10}$ @C composite materials for energy storage application is realized successfully by using the gelatins and $FeSO_4 \cdot 7\ H_2O$. Here, the fundamental approaches such as water-solvent, drying and carbonization are utilized to achieve this low-coast preparation. On the basis of observations of SEM morphologies, SAXD and BET evaluations, it is found that a lot of macropores and mesoporous structures exist in the fabricated $Fe_9S_{10}$ @C materials, while the $Fe_9S_{10}$ of the $Fe_9S_{10}$ @C composites is in nano sizes. The formations of complex pore structures facilitate the transfer of $Li^+$, which can lead the $Fe_9S_{10}$ @C to possess a tremendous electrochemical performance. For instance, the storage capacity of $Fe_9S_{10}$ @C-4.17 is 645.0 mAh $g^{-1}$ after cycling 100 times at 0.1 A $g^{-1}$. Additionally, the $Fe_9S_{10}$ @C-4.17 still show the storage capacity at 298.5 mAh $g^{-1}$, when carrying out the charge-discharge 200 cycles at 1 A $g^{-1}$. The present study may offer novel insights into the preparation of $Fe_9S_{10}$ @C materials with high electrochemical performance.

© 2023 Elsevier B.V. All rights reserved.

## 1. Introduction

With the vigorous development of energy storage systems (ESSs), the demands for electrodes with high storage capacity are becoming urgent more than ever before. Although the graphite and artificial graphite are extensively utilized in the fabrications of anodes of Lithium ion batteries (LiBs), their low theoretical capacity (372 mAh $g^{-1}$) exceedingly restricts their applications in the field of ESSs [1–3]. Therefore, developing the anode materials with high energy storage capacity is a pivotal subject for numerous of research groups and material makers for LIBs.

It is acknowledged that the anode fabrication processes of LIBs are mainly divided into three categories, according to the energy storage type of anode materials. i) It is a typical lithium intercalation type as representatives of graphite and artificial graphite [4]. ii) It is alloy-type as representatives of Si, Sn and P elements [5–9]. Considering the fact that the aforementioned elements own remarkable volumetric expansion in the discharge process, the fabrication of composites using the elements and carbons is a general method to overcome the aforementioned volumetric expansion problem. Recently, Si/C composites have received a lot of interests due to their excellent storage capacity. Nevertheless, the poor long-cycle performance restricts their applications in electrodes of LIBs [5–7]. iii) Conversion-type based on the conversion reaction usually exhibits relatively high storage capacity and electrochemical stability at high current density [10–18]. Therefore, a lot of metal oxides and metallic sulfides are developed as anode materials.

Based on the three comprehensive considerations such as cost-effectiveness, theoretical capacity and electrochemical stability, the conversion-type is preferred in our studies. In particular, the iron sulfide materials preferentially attracted our attention because they have some advantages such as being environmentally friendly and easily accessible in iron resources [14,17]. However, some demerits of volume expansion, long charger transmission distance and poor conductivity also restrict the actual applications of iron sulfide materials. To address the aforementioned demerits, the carbons having excellent conductivity are usually chosen to construct iron sulfide/C composites.

To date, composites constructed by iron sulfides (FeS, $FeS_2$, $Fe_3S_4$ and $Fe_7S_8$) with carbon materials are widely synthesized and developed [19–22]. These researches mainly focus on the designs of iron sulfides in nano sizes and morphologies of carbon materials. Nanocrystallization of iron sulfides can increase the reaction sites and shorten $Li^+$ diffusion distance to accelerate the reaction kinetic rate between $Li^+$ and iron sulfides. Similarly, the carbon covering method is also used to address the volumetric expansion problem of iron sulfides [20,22]. Especially, the carbon materials having complex structures can not only lead to efficacious electrolyte-electrode contact and decrease the interface charge transfer resistance, but also confined the volume changes of iron sulfides during the intercalation and deintercalation processes of $Li^+$. Nevertheless, the serious fabrication conditions also restrict the applications of the aforementioned methods. Therefore, fabricating iron sulfide@C composites having the high storage capacity by a simple method is an extremely fascinating research topic in the world.

Because of the fact that the $Fe_9S_{10}$ owns the high theoretical capacity (658.0 mAh/g) and excellent conductivity $10^2$-$10^3$ S $cm^{-1}$, it is also conceivably utilized to fabricate sulfide@C composites having high storage capacity in our studies [23]. Likewise, to develop the storage capacity of $Fe_9S_{10}$, a method covering the carbons on the surface of $Fe_9S_{10}$ is an effective way [23]. Because gelatin possesses a number of hydroxyl groups that are helpful for dispersing $Fe^{2+}$ of $FeSO_4·7 H_2O$, it is used as a carbon source to better disperse the fabricated $Fe_9S_{10}$ in carbon substrates [24]. The $Fe_9S_{10}$ in nano sizes in carbon substrates can remarkably increase the reaction kinetic rate between $Li^+$ and iron sulfides, leading to the enhancement of electrochemical performances of $Fe_9S_{10}$ @C materials [23]. Consequently, on the basis of a water-solvent method, the precursors of $Fe_9S_{10}$ @C materials are fabricated by using the $FeSO_4·7 H_2O$ and gelatin in our studies. After drying and carbonization procedures, the $Fe_9S_{10}$ @C materials are fabricated firstly and successfully. Meanwhile, the formations of Fe-O bonds between the gelatin based carbons and $Fe_9S_{10}$ can construct the conductive network, which effectively boosts the charge transfer around $Fe_9S_{10}$ and further develops the electrochemical performance of $Fe_9S_{10}$[22].

Herein, the electrochemical evaluations of $Fe_9S_{10}$ @C were performed in detail. After cycling 100 times at 0.1 A $g^{-1}$, it is observed that $Fe_9S_{10}$ @C-4.17 has the storage capacity of 645.0 $mAhg^{-1}$. In addition, the $Fe_9S_{10}$ @C-4.17 still exhibits the storage capacity of 298.5 $mAhg^{-1}$, when carrying out the charge-discharge 200 cycles at 1 A $g^{-1}$. The electrochemical results strongly suggest that $Fe_9S_{10}$ @C materials fabricated by $FeSO_4·7 H_2O$ and gelatin have a tremendous application prospect in ESSs.

## 2. Experimental section

### 2.1. Chemicals

The $FeSO_4·7H_2O$ (purity ≥ 99.7%) and gelatin (purity ≥ 99.5%) were purchased from Sinopharm Chemical Reagent Co., Ltd, P.R. China. All chemicals were used without any further purification.

### 2.2. Characteristics

The measurements of X-ray diffraction (XRD) and SAXD were performed by the X′pert Powder instrument from PANalytical. The X-ray photoelectron spectroscopy (XPS) measurements were carried out on a K-Alpha instrument from Thermo Fisher Scientific, USA. Nitrogen adsorption and desorption isotherms were measured by a Quadrasorbautosorb-iQ surface analyzer which was purchased from Quantachrome Instruments, USA. Specific surface areas were determined in detail, according to the Brunauer-Emmett-Teller (BET) method. The pore size distribution was assessed by a density functional theory (DFT) model for slit pores. Morphology was evaluated by transmission electron microscopy (TEM) using JEOL-JEM-2010 F instruments, Japan. LAND CT-3001A battery testing system was used to test the electrochemical performance of the buckle battery. Cyclic voltammetry (CV) and electrochemical impedance spectroscopy (over a frequency range of 100 kHz-0.01 Hz and the amplitude was 5 mV) were tested by CHI660E electrochemical workstation (ChenHua, Shanghai, China). Thermogravimetric (TGA) analysis (TG209F3, NETZSCH Group, Germany) was conducted from 30 ℃ to 800 ℃ at a heating rate of 10 ℃ per minute in air. Raman studies were performed using XploRA Plus Raman dispersive spectrometer (HORIBA Jobin Yvon, France). Conductivities of $Fe_9S_{10}$ @C materials were evaluated by ST-2258 C (Suzhou Lattice Electronics Co., Ltd, China).

### 2.3. Synthesis of $Fe_9S_{10}$@C composite materials

The gelatin (5 g) was respectively added to three beakers (50 mL) containing deionized water. The beakers were placed in water baths and stirred for 5 min at 70 ℃. The gelatins solutions became the transparent gel solutions with a color of light yellow. The $FeSO_4·7 H_2O$ (1.39 g, 4.17 g and 6.95 g) were added to the three beakers containing the fabricated transparent gel solution, and stirred for 10 min at 70 ℃. After cooling down to room temperature, the transparent gel solutions turned into solid colloidal substance, and the solid colloidal substances were dried at 80 ℃ for 12 h. After drying, the obtained materials were placed in the corundum porcelain boats, which were then put in the tube furnace and heated at 500 ℃ for 1 h in an $N_2$ atmosphere. The $Fe_9S_{10}$ @C composite materials were obtained at room temperature and named as $Fe_9S_{10}$ @C-1.39, $Fe_9S_{10}$ @C-4.17 and $Fe_9S_{10}$ @C-6.95, respectively, in accordance with different dosages of $FeSO_4·7 H_2O$.

### 2.4. Electrochemical measurements

The electrochemical properties of the $Fe_9S_{10}$ @C composites were evaluated by assembling CR2032 coin half cells in a glove box filled with argon (oxygen and moisture < 0.1 ppm). The lithium metal foil (φ 15.60 mm × 0.45 mm) as a reference electrode, Celgard 2400 micro-porous membrane as a separator, and 1 M $LiPF_6$ in the mixture of EC/DMC (1:1, vol%) with 5 vol% fluoroethylene carbonates (FEC) was applied as electrolyte. The working electrodes were composed of 80 wt% $Fe_9S_{10}$ @C materials, 10 wt% Super-P (conductive carbon), and 10 wt% polyvinylidenefluoride (PVDF) as the binder. N-Methyl-2-pyrrolidinone (NMP) was used as the solvent. The slurry obtained from the above mixed substances was coated on the Cu foil and then dried at 120 °C for 12 h in the vacuum drying oven, and Cu foil was cut into round shape strips of φ 11 mm in size, after cooling down to room temperature. The mass loading of the active materials was controlled at 1.67 mg/cm². A galvanostatic charge-discharge test was carried out by LAND (CT 3001 A) battery test system in the voltage range of 0.01–3.00 V. The CV curves were recorded in the voltage region of 0.01–3.00 V with a scan rate of 0.2 mV/s. The impedance spectra were recorded in a frequency range of 100 kHz - 0.01 Hz.
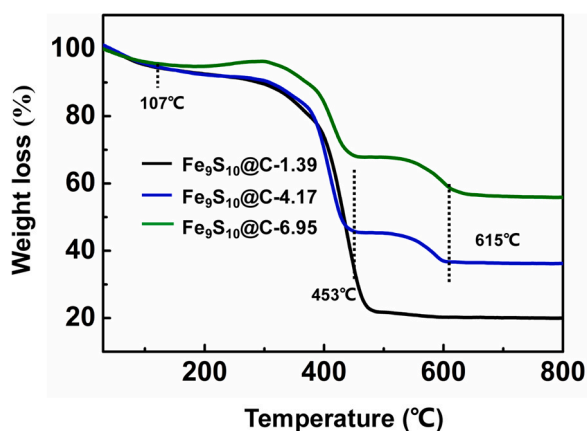
**Fig. 1.** TGA measurements of $Fe_9S_{10}$@C composite materials.

## 3. Results and discussion

First of all, the carbon contents in $Fe_9S_{10}$ @C composite materials were investigated, as shown in Fig. 1. The TGA measurements were performed at a temperature range of 30–800 °C in the air atmosphere. The mass decrease at 30 °C– 107 °C can be ascribed to the water loss, and a slight mass increase at 107 °C– 310 °C was attributed to that the $Fe_9S_{10}$ was partly oxidized to the $FeSO_4$ [25]. When the temperature was increased to 453 °C, the remarkable mass loss was ascribed to that the $Fe_9S_{10}$ was oxidized to the $Fe_2O_3$ and combustion of carbon [25]. The mass loss occurring at 615 °C can be ascribed to that $FeSO_4$ decomposed to the $Fe_2O_3$, $SO_2$ and $O_2$, respectively [25]. On the basis of reduced $Fe_2O_3$, the carbon contents of $Fe_9S_{10}$ @C-1.39, $Fe_9S_{10}$ @C-4.17 and $Fe_9S_{10}$ @C-6.95 were calculated at 77%, 58% and 35%, respectively.

The structures of $Fe_9S_{10}$ @C were confirmed by the XRD measurement results (Fig. 2). It is found that the 2θ degrees of 29.96°, 33.80°, 36.15° and 53.04° respectively corresponding to (201), (205), (118), (220) are consistent with ICDD 00–034–1470 of $Fe_9S_{10}$, indicating there is $Fe_9S_{10}$ in $Fe_9S_{10}$ @C composite materials [25,26]. In particular, the characteristic peak of carbons corresponding to the (002) at 25.61° can be observed after removing the $Fe_9S_{10}$ in $Fe_9S_{10}$ @C by using the HCl (1 M) (Fig. S1).

To elucidate the synthesis mechanism of $Fe_9S_{10}$ @C materials, the preparations were carried out by the reactions of $FeSO_4$·$7H_2O$ with and without gelatin at different heating temperatures with a same heating rate of 3.96 °C/min (Fig. 3). As shown in Fig. 3a, compared to the standard cards of $FeSO_4$·$H_2O$ and $FeSO_4$, it is observed that the $FeSO_4$ appeared at 400 °C. Furthermore, the $FeSO_4$·$H_2O$ completely
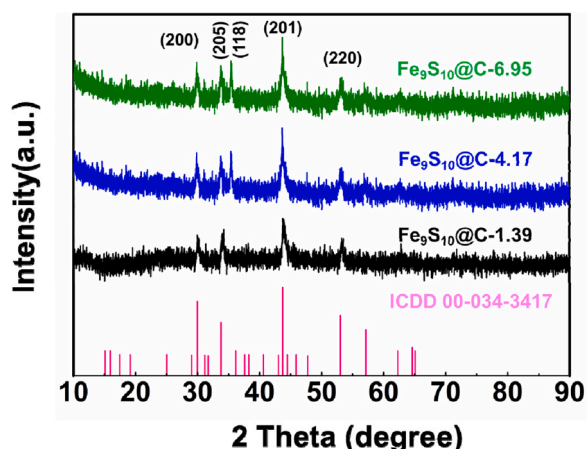


**Fig. 2.** XRD patterns of $Fe_9S_{10}$@C composite materials.

disappeared, and $FeSO_4$ formed thoroughly at 500 °C. However, the $Fe_9S_{10}$ is not observed in these heating processes.

Besides, in the preparation cases of $FeSO_4$·$7H_2O$ with gelatin, it is surprisingly observed that the structure of $FeSO_4$·$7H_2O$ broke, and a new structure attributing to the $Fe_9S_{10}$ appeared in the temperature range of (300 °C–400 °C) (Fig. 3b). In addition, it is found that the $Fe_9S_{10}$ clearly formed at 500 °C, and intensities of characteristic peaks of $Fe_9S_{10}$ significantly increased during 1 h in the continuously heating process. These results strongly suggest that gelatins participated in chemical reactions and promoted to the formation of $Fe_9S_{10}$ in $Fe_9S_{10}$ @C materials. All in all, it is interestingly observed that the formation of $Fe_9S_{10}$ requires the existence of gelatin in our synthesis cases. Namely, the reactions of two contents of $FeSO_4$·$7H_2O$ and gelatins lead to the formation of $Fe_9S_{10}$ in carbon substrates at 500 °C.

The aforementioned fact that gelatin participated in the synthesis reactions indicates that the gelatin should have an impact on the structure of $Fe_9S_{10}$. In addition, it is interestingly observed that the intensity of a peak at 36.15° increased with increasing the dosages of $FeSO_4$·$7H_2O$, which is probably attributed to the influence from carbons on $Fe_9S_{10}$ decreases gradually (Fig. 2). The similar phenomenon is also explained by Yuan et. al., who fingered out that adding small organic molecules can control the free energy of different crystal planes [27].

To further discuss the structure of $Fe_9S_{10}$ @C materials, the Raman measurements were performed (Fig. 4). In general, the D peak attributing to the defects on the graphite edge and G peak from the $sp^2$ structures on carbon shits were observed at 1355 $cm^{-1}$ and 1600 $cm^{-1}$, respectively. To investigate the structures of $Fe_9S_{10}$ @C materials correctly, the peak fitting was conducted in detail, and area ratios of $A_G$/$A_D$ of G peak and D peak of $Fe_9S_{10}$ @C-1.39, $Fe_9S_{10}$ @C-4.17 and $Fe_9S_{10}$ @C-6.95 are calculated as 1.970, 1.971 and 1.971, respectively, indicating the added $Fe_9S_{10}$ did not influence the microcrystal structures of carbon substrates approximately [23]. Especially, the characteristic peaks of $Fe_9S_{10}$ are not observed obviously in Raman spectra, which is probably attributed to that the $Fe_9S_{10}$ is encapsulated by gelatin based carbons (Fig. 4) [28].

To inquire into the chemical states, the XPS measurements were carried out in detail (Fig. 5 and Fig.S2-S4). As shown in Fig. S2, the five characteristic peaks attributing to the C, O, S, N and Fe are observed at 284.6 eV (C 1 s), 530.8 eV (O 1 s), 228.6 eV (S 2 s), 164.6 eV (S 2p), 398.1 eV (N 1 s) and 711.1 eV (Fe 2p) respectively. Additionally, the detailed chemical states in $Fe_9S_{10}$ @C composites were analyzed by a fitting method. In C 1 s fitting peaks, the C-C bonds were observed at 284.3 eV and the C-O, and C=O bonds were around 285.5 eV and 288.1 eV, respectively [29–32] (Fig. 5a). The presences of C-O and C=O bonds are thought to be advantageous for immobilizing the $Fe_9S_{10}$ and beneficial in the construction of a conductive network between carbons and $Fe_9S_{10}$. Fig. 5b exhibits that the peaks of 529.4, 531.0 and 532.9 eV correspond to the Fe-O, C-O and O-C=O bonds respectively [29,33]. The Fe-O bond reveals that the interactions between the carbon and $Fe_9S_{10}$ exist certainly, which is beneficial to develop the storage characteristic of $Fe_9S_{10}$ better [29]. In S 2p fitting peaks, the $S^{2-}$ characteristic peak was observed at 160.9 eV, and the peaks of $S_n^{2-}$ and S $2p_{1/2}$ were observed at 163.3 eV and 167.9 eV, respectively (Fig. 5c) [19–22]. Fig. 5d illustrates the fitting peaks of Fe 2p. It is found that the peaks of 712.7 eV and 724.1 eV are ascribed to $Fe^{3+}$, and a peak of 710.1 eV can be definitively attributed to the $Fe^{2+}$, which provides absolute proof for the existence of $Fe_9S_{10}$ [23,34]. Additionally, the elements contents in $Fe_9S_{10}$ @C materials were calculated and illustrated in the Table S2. It is distinctly aware of that the atomic proportions of C, N and O elements diminished with increasing the contents of Fe (Table S2). A similar tendency is also verified by elemental analysis measurements (Table S3).
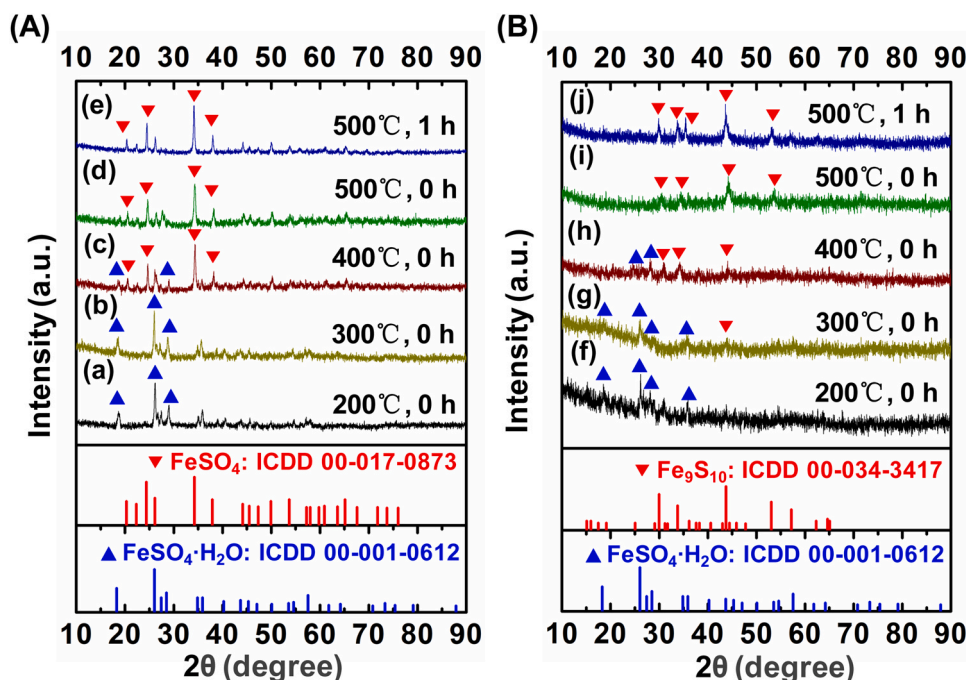
**Fig. 3.** (A) XRD results of FeSO$_4$·7H$_2$O deal with at different temperatures. (a~d) are the cases, where the heating temperatures increased from room temperature to 200, 300, 400, 500 ℃ with the heating rate of 3.96 ℃/min. The heating temperature was increased to the 500 ℃ with the heating rate of 3.96 ℃/min, and maintained for 1 h at 500 ℃ (e). (B) XRD results of products by reactions of FeSO$_4$·7H$_2$O with gelatins. (f~i) are the cases, in which the reactive temperatures increased from room temperature to 200, 300, 400, 500 ℃ with the heating rate of 3.96 ℃/min. The reactive temperature was increased to the 500 ℃ with the heating rate of 3.96 ℃/min, and maintained for 1 h at 500 ℃ (j).
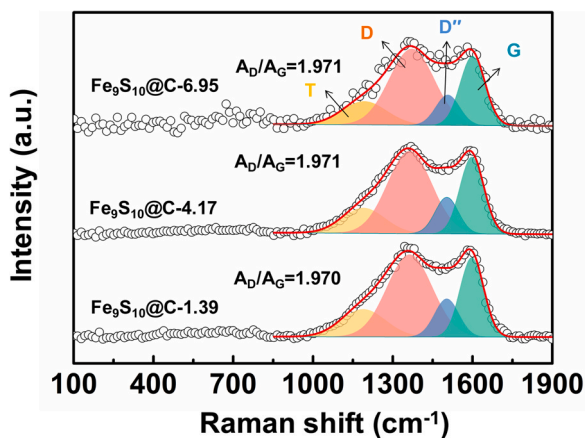


**Fig. 4.** Raman results of Fe$_9$S$_{10}$@C materials.

The morphologies of Fe$_9$S$_{10}$ @C materials were investigated by the SEM and TEM measurements. Compared to the carbons obtained from gelatins and Fe$_9$S$_{10}$ @C-1.39, it is distinct that the porous structures obviously appeared on the surfaces of Fe$_9$S$_{10}$ @C-4.17 and Fe$_9$S$_{10}$ @C-6.95 (Fig. S5). Besides, in TEM morphologies, it is observed that carbons clearly encapsulated the Fe$_9$S$_{10}$ (Fig. 6a-b), and the interplanar spaces of 0.282 nm, 0.248 nm and 0.298 nm corresponding to the three planes of (109), (118) and (200), were clearly observed respectively (Fig. 6c). TEM morphologies effectively suggest the structure of Fe$_9$S$_{10}$ in Fe$_9$S$_{10}$ @C materials [23,26]. Meanwhile, it can be seen that Fe and S possess homogeneous distributions in the carbon substrates, indicating Fe$_9$S$_{10}$ nano-sized particles dispersed in carbon substrates better (Fig. 6d). In addition, it is interestingly aware of that the nitrogen element exists, and distributes homogeneously, which is brought by gelatins (Fig. 6d). The existence of nitrogen element is able to be the key component for accelerating the infiltration of electrolyte and Li$^+$ transfer [35–37].

The BET methods were used to investigate the specific surface areas and porous structures of Fe$_9$S$_{10}$ @C composite materials (Figs. 7a and 7b). It is distinct that all samples show a type IV isotherm with type H3 hysteresis loops, indicating the presence of mesoporous structures. Additionally, an observation that the hysteresis loops shift to a relatively high pressure region with increment of dosages of FeSO$_4$·7 H$_2$O reveals the existences of macropores in Fe$_9$S$_{10}$ @C-4.17 and Fe$_9$S$_{10}$ @C-6.95 materials [32]. The existences of a number of mesoporous and macropores are able to boost the Li$^+$ transfer, causing an improvement in the rate performances. As shown in Table S1, the specific surface areas and pore volumes increased with increasing dosages of FeSO$_4$·7 H$_2$O, which is likely due to the fact that adding more FeSO$_4$·7 H$_2$O can speed up the decomposition of gelatin in carbonization cases [11]. Namely, the dispersions of Fe$_9$S$_{10}$ particles in substrates in nano sizes can facilitate this decomposition of gelatins [38]. However, compared with the Fe$_9$S$_{10}$ @C-4.17, the increase in the specific surface area of Fe$_9$S$_{10}$ @C-6.95 is not obvious, which is probably attributed to that the agglomeration phenomenon among the Fe$_9$S$_{10}$ particles decreased their dispersions in substrates.

Furthermore, the porous structures are further analyzed by small angle x-ray diffraction (SAXD) (Fig. S6). Similar to reports by Xie et. al., the pore sizes of ordered porous of Fe$_9$S$_{10}$ @C-1.39, Fe$_9$S$_{10}$ @C-4.17 and Fe$_9$S$_{10}$ @C-6.95 are 14.41 nm , 21.52 nm and 11.44 nm, respectively, indicating that the Fe$_9$S$_{10}$ @C-4.17 possesses bigger ordered porous than that of Fe$_9$S$_{10}$ @C-1.39 and Fe$_9$S$_{10}$ @C-6.95 [39,40]. These results are probably ascribed to the excellent dispersions of Fe$_9$S$_{10}$ @C-4.17 with nano sizes.

The electrochemical performances of Fe$_9$S$_{10}$ @C composite materials are illustrated in Fig. 8. Fig. 8a shows that the storage capacity of Fe$_9$S$_{10}$ @C-4.17 is 645.0 mAh g$^{-1}$ after cycling 100 times, which is higher than that of Fe$_9$S$_{10}$ @C-1.39 (156.1 mAh g$^{-1}$), Fe$_9$S$_{10}$ @C-6.95 (313.8 mAh g$^{-1}$) and carbon (303.8 mAh g$^{-1}$), respectively. In addition, after cycling 200 times, the Fe$_9$S$_{10}$ @C-4.17 still has the storage capacity of 298.5 mAh g$^{-1}$ at a big current density of 1 A g$^{-1}$, indicating that Fe$_9$S$_{10}$ @C-4.17 owns an excellent long cycle
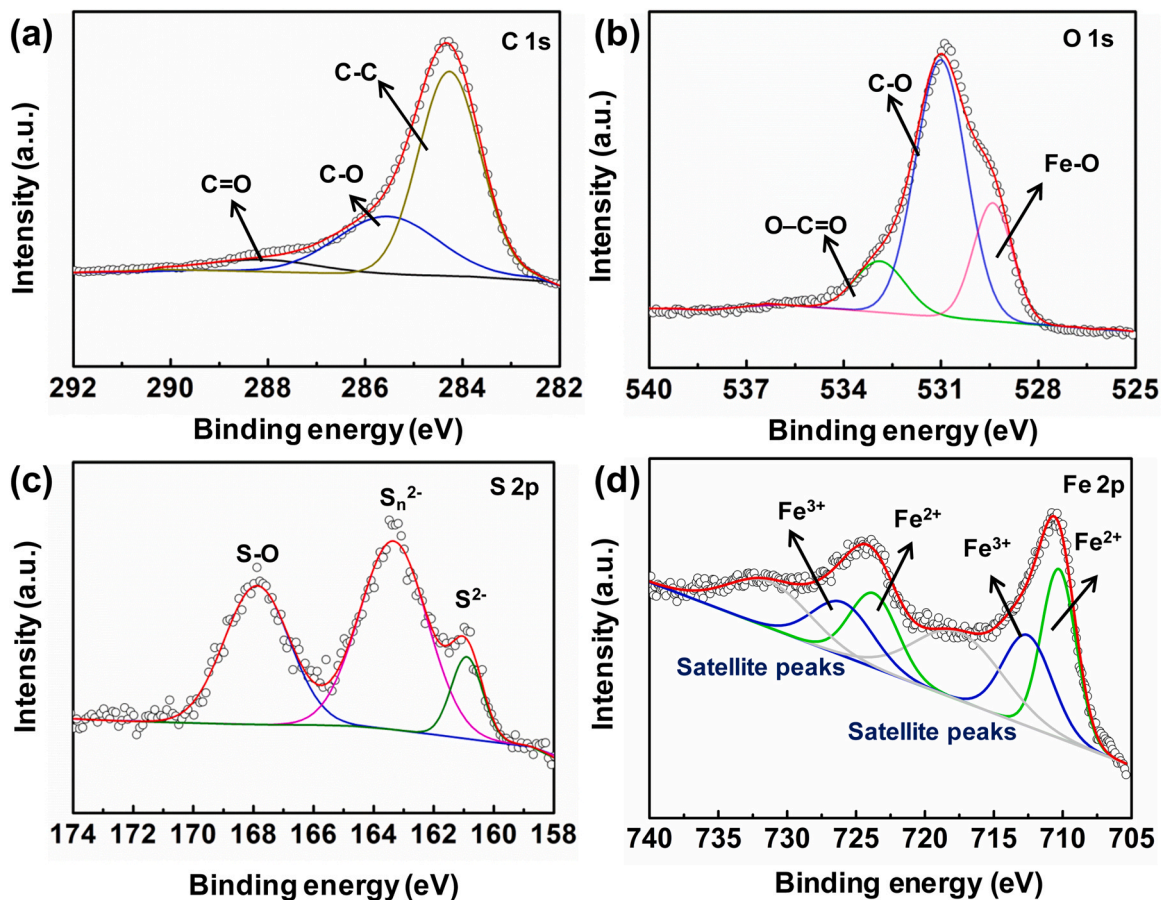
**Fig. 5.** XPS spectra of $Fe_9S_{10}$@C-4.17 composite materials. C 1 s spectrum (a), O 1 s spectrum (b), S 2p spectrum (c), Fe 2p spectrum (d).
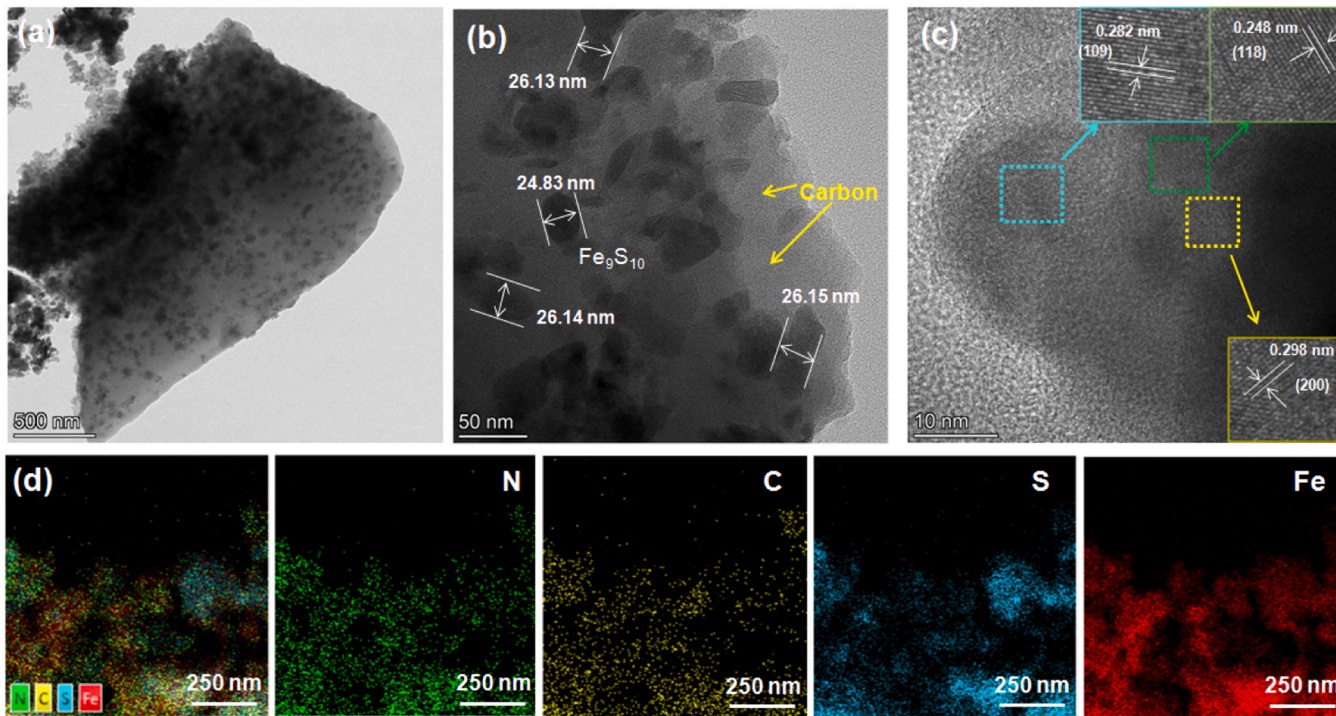


**Fig. 6.** TEM-images and TEM-EDX images of $Fe_9S_{10}$ @C-4.17. TEM images (a, b), HRTEM images (c), TEM-EDX images (d).
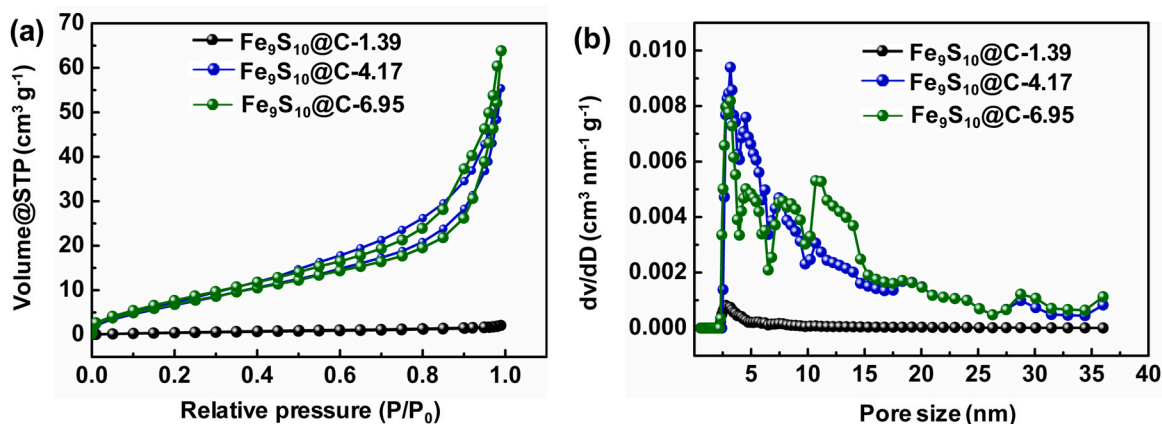
**Fig. 7.** Nitrogen adsorption desorption isotherms (a) and pore size distributions of $Fe_9S_{10}$ @C composite materials (b).

performance (Fig. 8c). Meanwhile, the $Fe_9S_{10}$ @C-4.17 manifests the more tremendous rate performance than the others (Fig. 8b).

To explore the electrochemical reactions of $Fe_9S_{10}$ @C composite materials, the CV measurements were conducted in detail (Fig. 9a-c). For the first round cycles, the reductive peaks of 0.56 V, 0.67 V and 0.63 V attributing to the formations of solid electrolyte interface (SEI) were respectively assigned to the $Fe_9S_{10}$ @C-1.39, $Fe_9S_{10}$ @C-4.17 and $Fe_9S_{10}$ @C-6.95 [19]. Additionally, the reductive peaks of $Fe_9S_{10}$ @C-1.39, $Fe_9S_{10}$ @C-4.17 and $Fe_9S_{10}$ @C-6.95 were respectively observed at 1.25 V, 1.13 V and 1.14 V [20], which were attributed to a process that $Fe^{3+}$ was reduced to the $Fe^{2+}$. It is considerable that the weak peaks of 1.51 V, 1.64 V and 1.65 V correspond to the formation of $Li_2FeS_2$ by a reaction of $Li^+$ with $Fe_9S_{10}$ [21]. The oxidative peaks of 1.94 V, 1.97 V and 1.94 V are attributed to a transformation of $Fe^0$ to $Li_2FeS_2$ (Fig. 9a-c).

In the following two cycles of a reduction process, the reductive peaks of 1.25 V and 1.14 V corresponding to the $Fe_9S_{10}$ @C-1.39 and $Fe_9S_{10}$ @C-6.95 shifted to the 1.34 V and 1.36 V, respectively (Fig. 9a and c). However, a peak of 1.33 V of $Fe_9S_{10}$ @C-4.17 did not change approximately, indicating that adequate carbon contents in $Fe_9S_{10}$ @C-4.17 can lead the $Fe_9S_{10}$ to develop its storage capacity best (Fig. 9b).

The charge-discharge curves (Fig. 9d-f) show that the initial discharge/charge capacities of $Fe_9S_{10}$ @C-1.39, $Fe_9S_{10}$ @C-4.17 and $Fe_9S_{10}$ @C-6.95 are 872.0/415.0, 1180.2/742.0, and 1116.3/788.6 mAh $g^{-1}$, with coulombic efficiencies of 47.6%, 62.9% and 70.6%, respectively. It is aware of that the charge-discharge plateaus are 0.56 V, 0.67 V and 0.63 V in the first cycle, which correspond to their reductive peaks in the first cycle of CV results. Additionally, the charge-discharge plateaus at 0.67 V and 0.63 V of $Fe_9S_{10}$ @C-4.17 and $Fe_9S_{10}$
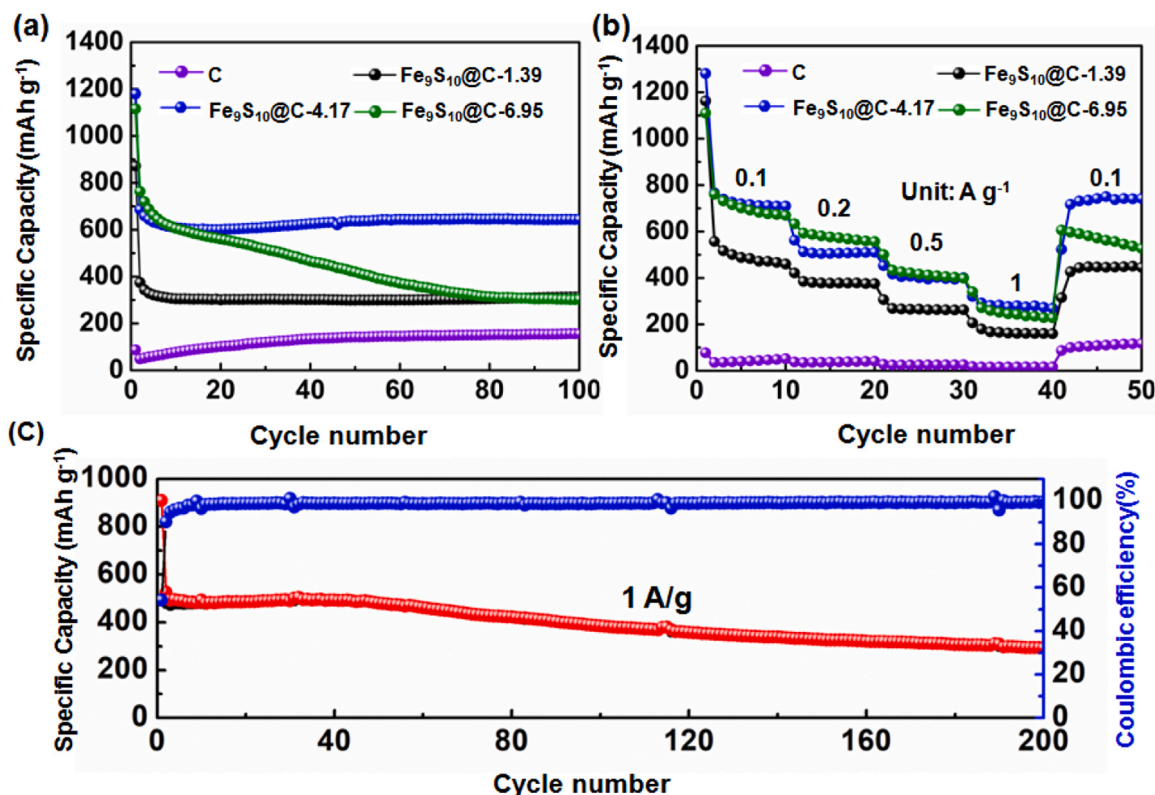


**Fig. 8.** Cycling performances of $Fe_9S_{10}$@C composite materials and C (a). Rate performances of $Fe_9S_{10}$ @C composite materials and C (b). Storage capacity of $Fe_9S_{10}$@C-4.17 at 1.0 A $g^{-1}$ after 200 cycles (c).

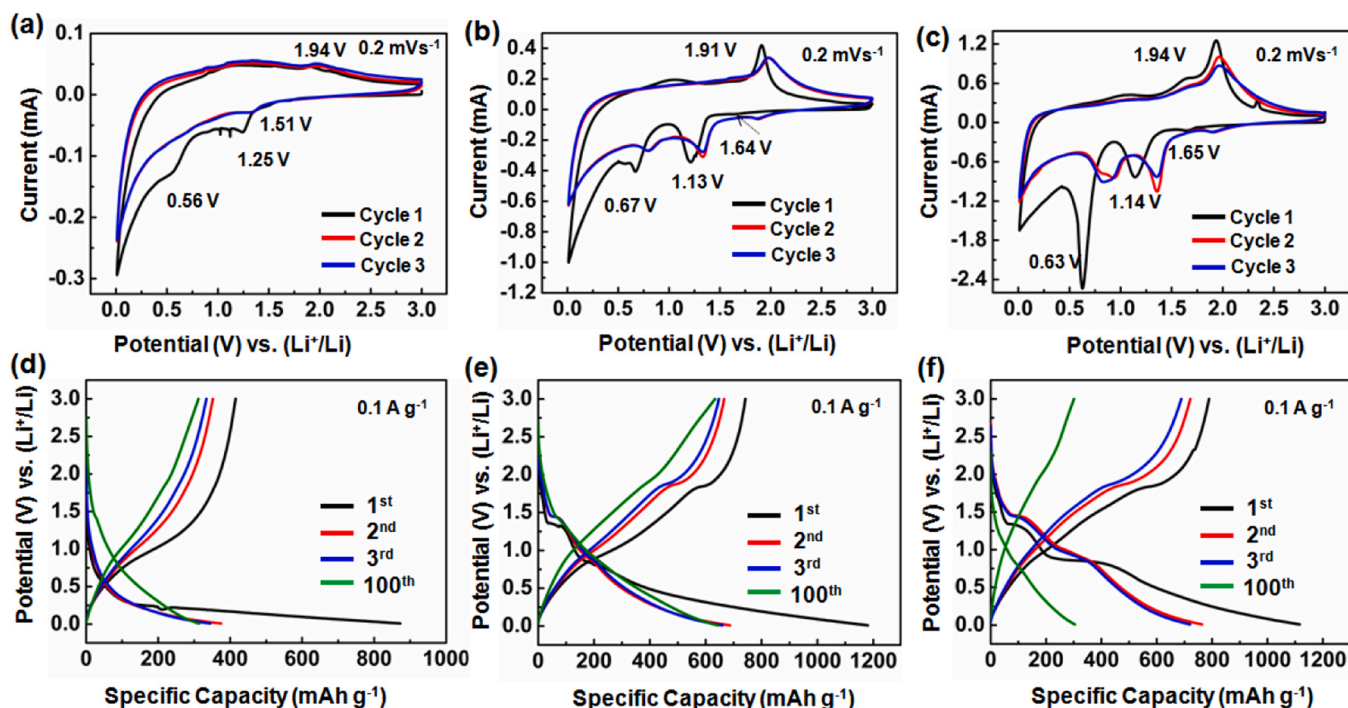**Fig. 9.** CV curves for the first 3 cycles of $Fe_9S_{10}$@C-1.39 electrode, $Fe_9S_{10}$@C-4.17 electrode and $Fe_9S_{10}$@C-6.95 electrode, respectively (a-c), GCD profiles of $Fe_9S_{10}$@C-1.39 electrode, $Fe_9S_{10}$@C-4.17 electrode and $Fe_9S_{10}$@C-6.95 electrode, respectively (d-f).
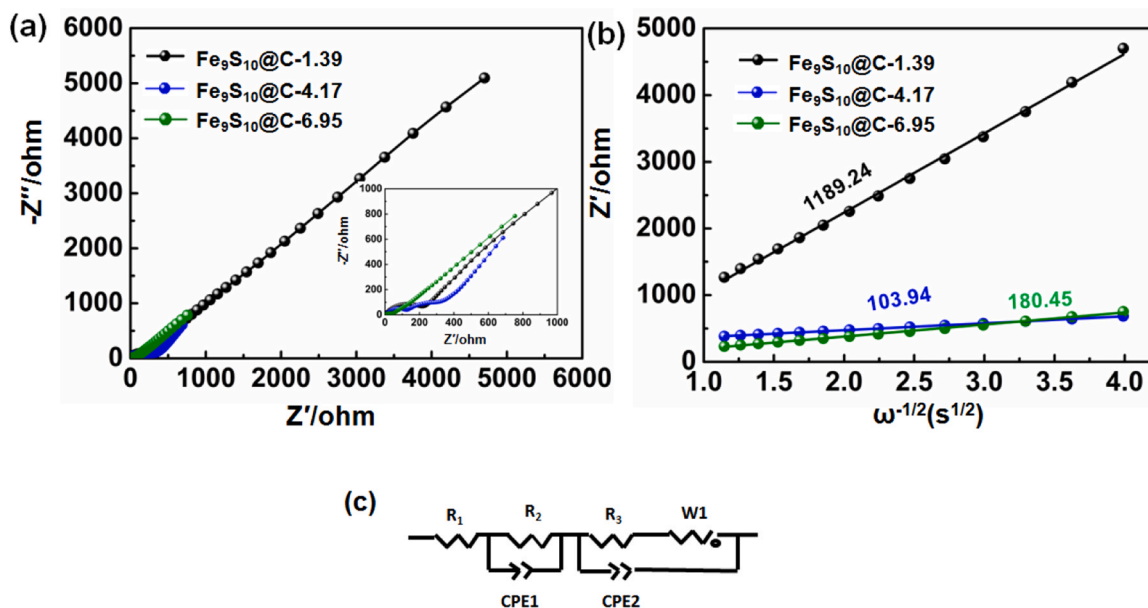


**Fig. 10.** Nyquist plots of $Fe_9S_{10}$@C electrodes at potential voltage around 2.2 V (a), illustrations of relationships between Z′ and $\omega^{-1/2}$ in the low-frequency region (b) and the equivalent Randles circuit (c). Thereinto, $R_1$ is the total resistance of the electrolyte, separator, and electrical contacts; $R_2$ and $R_3$ are the $Li^+$ migration resistance through the SEI film and charge-transfer resistance, respectively; W1 is the Warburg impedance connected with the $Li^+$ diffusion process; CPE1 and CPE2 represent the double layer resistance.

@C-6.95 are wider than the $Fe_9S_{10}$ @C-1.39, which are relative to that $Fe_9S_{10}$ @C-4.17 and $Fe_9S_{10}$ @C-6.95 possess the bigger specific surface area than $Fe_9S_{10}$ @C-1.39, causing the widely forming of SEI [19].

The conductivities of $Fe_9S_{10}$ @C powders were evaluated by the four probe method. As shown in Table S4, it is distinct that the conductivities increase with the additional amount of $Fe_9S_{10}$, which attributes to the excellent conductivity of $Fe_9S_{10}$ ($10^2$-$10^3$ S cm$^{-1}$) (Table S5) [23]. In order to clarify the reason why the $Fe_9S_{10}$ @C-4.17 manifests the fabulous electrochemical performance, the electrochemical impedance spectroscopy (EIS) measurements were carried out in detail. Fig. 10a manifested that $Fe_9S_{10}$ @C-4.17 possesses the smaller diameters of semicircle loop at high frequency region than $Fe_9S_{10}$ @C-1.39 and $Fe_9S_{10}$ @C-6.95, indicating that the $Fe_9S_{10}$ @C-4.17 possesses the more tremendous transfer abilities than the others. Based on the artificial circuit, the $R_3$ values of $Fe_9S_{10}$ @C-1.39, $Fe_9S_{10}$ @C-4.17 and $Fe_9S_{10}$ @C-6.95 were calculated at 1104.0 $\Omega$, 146.1 $\Omega$ and 262.9 $\Omega$, respectively, revealing that $Fe_9S_{10}$ @C-4.17 owned a more excellent conductivity than other materials (Table S6).
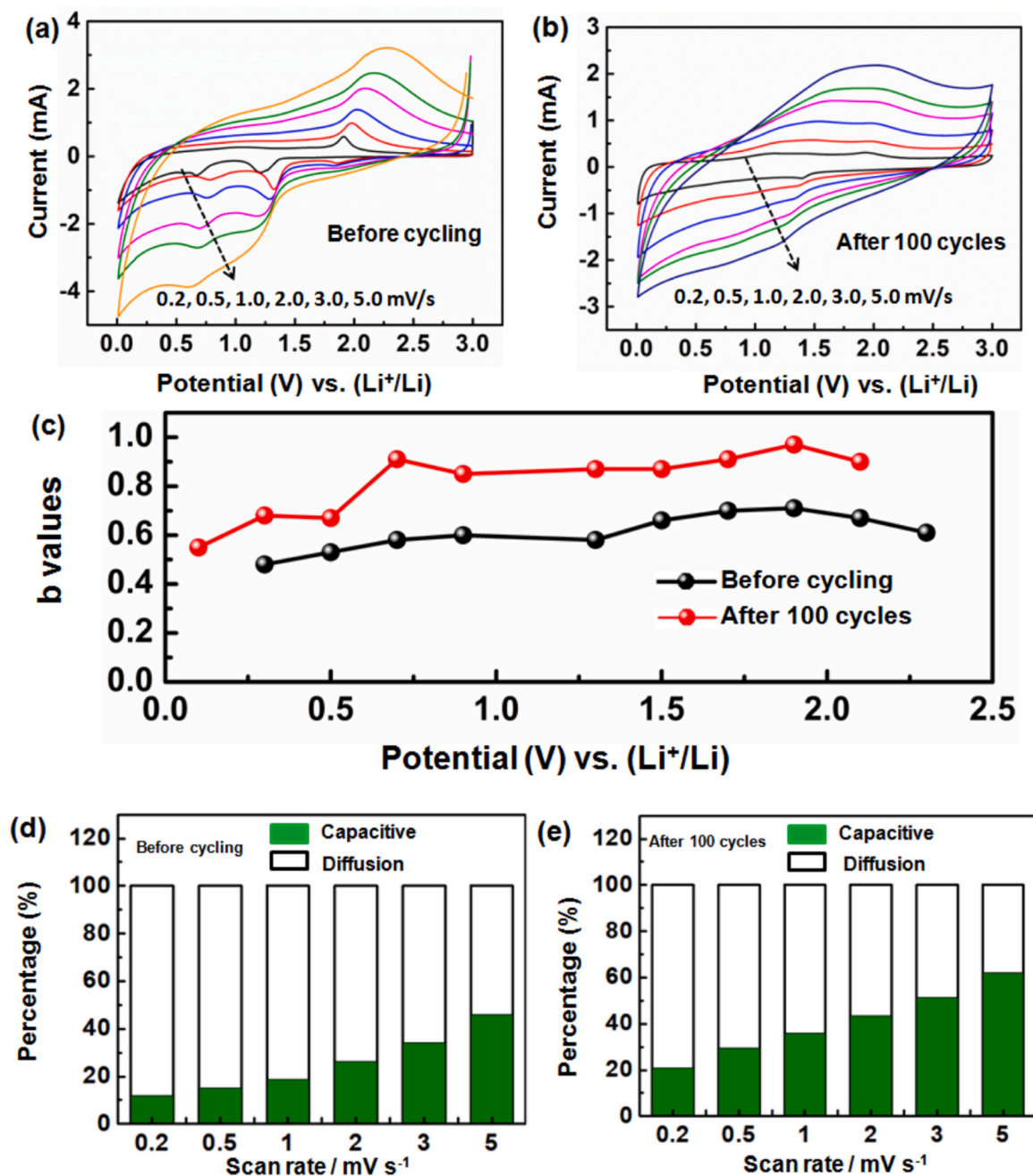
**Fig. 11.** CV curves of $Fe_9S_{10}$@C-4.17 electrode at different scan rates. Before cycling (a). After 100 cycles (b). b values before and after 100 cycles for $Fe_9S_{10}$@C-4.17 electrode during the discharge process (c). Capacitive contributions of $Fe_9S_{10}$@C-4.17 before cycling at different scan rates (d). Capacitive contributions of $Fe_9S_{10}$@C-4.17 after cycling at different scan rates (e).

In addition, the diffusions of $Li^+$ were generally verified by $\sigma$ (Warburg coefficient), similar to the report by Zheng et. al [41] (Fig. 10b). The smaller $\sigma$ values indicate that the materials have the more excellent $Li^+$ transfer ability than others. After calculations, the $\sigma$ values of $Fe_9S_{10}$@C-1.39, $Fe_9S_{10}$@C-4.17 and $Fe_9S_{10}$@C-6.95 were 1189.24 $\Omega\,s^{1/2}$, 103.94 $\Omega\,s^{1/2}$ and 180.45 $\Omega\,s^{1/2}$, respectively. These results suggest that $Fe_9S_{10}$@C-4.17 possesses an excellent $Li^+$ transfer ability, compared with that in other materials (Table S6). In particular, similar to the reports, the Z′ was calculated and illustrated in Table S6. It is found that the Z′ for $Fe_9S_{10}$@C-1.39 is significantly higher than that of $Fe_9S_{10}$@C-4.17 and $Fe_9S_{10}$@C-6.95. Associated with the BET results, it is thought that a smaller specific surface area is a probable reason which causes that $Fe_9S_{10}$@C-1.39 possesses a higher $Z_{re}$ value than that of $Fe_9S_{10}$@C-4.17 and $Fe_9S_{10}$@C-6.95

[42,43]. On the basis of the aforementioned analyses, it is considerable that the excellent conductivity and $Li^+$ transfer ability of $Fe_9S_{10}$@C-4.17 lead it to possess more tremendous electrochemical performance than $Fe_9S_{10}$@C-4.17, $Fe_9S_{10}$@C-6.95 and other reported compounds (Table S7).

To elucidate the storage mechanism of $Fe_9S_{10}$@C-4.17 better, the dynamics analyses were conducted in detail. Compared with Fig. 11a, the CV behaviors of $Fe_9S_{10}$@C-4.17 manifest the rectangle shaped tendency, indicating that the half cells in different states such as before cycling and after 100 cycles have different storage types. Namely, the contributions of the capacitance effect gradually increase after 100 cycles.

Similar to the report by Zhang et al., the b values obtained by the formula of $i = a\upsilon^b$ were used to analyze the storage types of $Fe_9S_{10}$

@C-4.17 [44]. In general, the b values belonging to a range of (0.5–7.5) reveal that the storage type of materials is the intercalation type. Besides, if the b values are getting closer to 1.0, the storage type of materials most likely tends to be a capacitive type. After carrying out calculations, it is obvious that the storage type of $Fe_9S_{10}$ @C-4.17 exhibits an intercalation type before cycling. By contrast, the capacitive effect plays the main contribution to the storage capacity after cycling 100 times. The changes in storage type are probably attributed to the structural conversions of nano-sized $Fe_9S_{10}$, with the proceeding of the electrochemical activation [45,46].

Furthermore, similar to the report by Wang et. al., the capacitive contribution and diffusion-controlled contributions were calculated by a formula of $I(V) = k_1\upsilon + k_2\upsilon^{1/2}$ (The $k_1\upsilon$ represents the contribution of the capacitive process, whereas $k_2\upsilon^{1/2}$ indicates the contribution of the diffusion-controlled process) [40]. As a result, it is found that the capacitive contributions rose with increasing the scan rates Fig. 11d and e. Especially, the enhancement of capacitive contributions of $Fe_9S_{10}$ @C-4.17 after 100 cycles is more remarkable than that of $Fe_9S_{10}$@C-4.17 before cycling.

## 4. Conclusions

The $Fe_9S_{10}$@C composites were successfully fabricated by the gelatin and $FeSO_4 \cdot 7 H_2O$. It is found that the gelatin are help to disperse the $Fe_9S_{10}$ in nano sizes. The porous structures constructed by the mesoporous and macropores are beneficial to improve the charge transfer, causing the enhancement of the storage capacity of $Fe_9S_{10}$@C composites. As a result, after cycling 100 times at $0.1\,A\,g^{-1}$, $Fe_9S_{10}$@C-4.17 has the storage capacity of 645.0 mAhg$^{-1}$. In addition, the $Fe_9S_{10}$@C-4.17 still exhibits the storage capacity of 298.5 mAh g$^{-1}$, when carrying out the charge-discharge 200 cycles at $1\,A\,g^{-1}$. The electrochemical performances indicate that simply fabricated $Fe_9S_{10}$@C materials possess excellent application prospects.

## Declaration of Competing Interest

The authors declare that they have no known competing financial interests or personal relationships that could have appeared to influence the work reported in this paper.

## Acknowledgements

## Appendix A. Supporting information

Supplementary data associated with this article can be found in the online version at doi:10.1016/j.jallcom.2023.169442.

## References

[1] V. Aravindan, Y. Lee, S. Madhavi, Research progress on negative electrodes for practical li-ion batteries: beyond carbonaceous anodes, Adv. Energy Mater. 5 (2015) 1402225.

[2] J. Hou, S. Qu, M. Yang, J. Zhang, Materials and electrode engineering of high capacity anodes in lithium ion batteries, J. Power Sources 450 (2020) 227697.

[3] Y. Cheng, Y. Sun, C. Chu, L. Chang, Z. Wang, D. Zhang, W. Liu, Z. Zhuang, L. Wang, Stabilizing effects of atomic Ti doping on high-voltage high-nickel layered oxide cathode for lithium-ion rechargeable batteries, Nano Res. 15 (2022) 4091–4099.

[4] B. Babu, P. Simon, A. Balducci, Fast charging materials for high power applications, Adv. Energy Mater. 29 (2020) 2001128.

[5] W. Liu, J. Liu, M. Zhu, W. Wang, L. Wang, S. Xie, L. Wang, X. Yang, X. He, Y. Sun, Recycling of lignin and Si waste for advanced Si/C battery anodes, ACS Appl. Mater. Interfaces 12 (2020) 57055–57063.

[6] R. Shao, J. Nin, F. Zhu, M. Dou, Z. Zhang, F. Wang, A facile and versatile strategy towards high-performance Si anodes for Li-ion capacitors: concomitant conductive network construction and dual-interfacial engineering, Nano Energy 63 (2019) 103824.

[7] S. Yeom, C. Lee, S. Kang, T.U. Wi, C. Lee, S. Chae, J. Cho, D. Shin, J. Ryu, H.W. Lee, Native void space for maximum volumetric capacity in silicon-based anodes, Nano Lett. 19 (2019) 8793–8800.

[8] W. Lv, T. Wang, H. Qiu, Sn nanoparticles anchored on carbon foam prepared by a facile electrodeposition for lithium storage, Energy Technol. 12 (2022) 202200789.

[9] L. Sun, Y. Zhang, Y. Gong, H. Si, Y. Shi, K. Fan, C. Sun, Y. Zhang, Sn-Decorated red P entangled in CNTs as anodes for advanced lithium ion batteries, Dalton Trans. 49 (2020) 10909–10917.

[10] H. Wang, S. Chen, S. Fu, Y. Ding, G. Liu, Y. Cao, Z. Chen, Recent advances in conversion-type electrode materials for post lithium-ion batteries, ACS Mater. Lett. 3 (2021) 956–977.

[11] K. Wang, D. Ju, G. Xu, Y. Wang, S. Chen, J. Zhang, Y. Wu, W. Zhou, Study on electrochemical performances of composite carbon (FeO/C) materials fabricated by coal tar pitch and $Fe_3O_4$ particles, Int. J. Hydrog. Energy 44 (2019) 25199–25206.

[12] K. Cao, T. Jin, L. Yang, L. Jiao, Recent progress in conversion reaction metal oxide anodes for Li-ion batteries, Mater. Chem. Front. 1 (2017) 2213–2242.

[13] S. Hu, F. Yin, E. Uchaker, M. Zhang, W. Chen, J. Zhou, Y. Qi, G. Cao, Facile and green preparation for the formation of $MoO_2$-GO composites as anode material for lithium-ion batteries, J. Phys. Chem. C. 118 (2014) 24890–24897.

[14] Q. Zhang, X. Yao, J. Mwizerwa, N. Huang, H. Wang, Z. Huang, X. Xu, FeS nanosheets as positive electrodes for all-solid-state lithium batteries, Solid State Ion. 318 (2018) 60–64.

[15] M.J. Xiao, B. Ma, H. Zhang, X.Y. Li, Q. Wang, Y. Peng, H.L. Zhang, Hollow NiO/carbon pompons for efficient lithium ion storage, J. Mater. Chem. A 10 (2022) 21492–21502.

[16] Y. Yan, Y. Liu, Y. Zhang, C. Qin, H. Yu, Z. Bakenov, Z. Wang, Sn modified nanoporous Ge for improved lithium storage performance, J. Colloid Interface Sci. 602 (2021) 563–572.

[17] W.J. Yu, C. Liu, L. Zhang, P.X. Hou, F. Li, B. Zhang, H.M. Cheng, Synthesis and electrochemical lithium storage behavior of carbon nanotubes filled with iron sulfide nanoparticles, Adv. Sci. 3 (2016) 1600113.

[18] Q. Ma, Q. Zhuang, J. Liang, Z. Zhang, J. Liu, H. Peng, C. Mao, G. Li, Novel mesoporous flowerlike iron sulfide hierarchitectures: Facile synthesis and fast lithium storage capability, Nanomaterials 7 (2017) 431.

[19] S. Li, B. Qu, H. Huang, P. Deng, C. Xu, Q. Li, T. Wang, Controlled synthesis of iron sulfide coated by carbon layer to improve lithium and sodium storage, Electrochim. Acta 247 (2017) 1080–1087.

[20] J. Zhao, Z. Hu, D. Sun, H. Jia, X. Liu, MOF-derived FeS/C nanosheets for high performance lithium ion batteries, Nanomaterials 9 (2019) 492.

[21] S. Khateeb, T. Sparks, Spray pyrolysis of conductor-and binder-free porous $FeS_2$ films for high-performance lithium ion batteries, J. Mater. Sci. 54 (2019) 4089–4104.

[22] Q.T. Xu, J.C. Li, H.G. Xue, S.P. Guo, Effective combination of $FeS_2$ microspheres and $Fe_3S_4$ microcubes with rGO as anode material for high-capacity and long-cycle lithium-ion batteries, J. Power Sources 396 (2018) 675–682.

[23] Z. Xu, Z. Wang, M.R. Wang, H.T. Cui, Y.Y. Liu, H.Y. Wei, J. Li, Large-scale synthesis of $Fe_9S_{10}$/$Fe_3O_4$@C heterostructure as integrated trapping-catalyzing interlayer for highly efficient lithium-sulfur batteries, Chem. Eng. J. 422 (2021) 130049.

[24] Z. Schnepp, S. Wimbush, M. Antonietti, C. Giordano, Synthesis of highly magnetic iron carbide nanoparticles via a biopolymer route, Chem. Mater. 22 (2010) 5340–5344.

[25] C. Zhang, F. Han, J. Ma, Z. Li, F. Zhang, S. Xu, H. Liu, X. Li, J. Liu, A.H. Lu, Fabrication of strong internal electric field ZnS/$Fe_9S_{10}$ heterostructures for highly efficient sodium ion storage, J. Mater. Chem. A 7 (2019) 11771–11781.

[26] X.X. Ma, Y. Su, X.Q. He, $Fe_9S_{10}$-decorated N, S co-doped graphene as a new and efficient electrocatalyst for oxygen reduction and oxygen evolution reactions, Catal. Sci. Technol. 7 (2017) 1181–1192.

[27] Q.L. Yuan, P.F. Li, J. Liu, Y. Lin, Y.Y. Cai, Y.X. Ye, C.H. Liang, Facet-Dependent selective adsorption of Mn-Doped $\alpha$-$Fe_2O_3$ nanocrystals toward heavy-metal ions, Chem. Mater. 29 (2017) 10198–10205.

[28] C. Zhang, F. Han, F. Wang, Q. Liu, D. Zhou, F. Zhang, S. Xu, C. Fan, X. Li, J. Liu, Improving compactness and reaction kinetics of $MoS_2$@C anodes by introducing $Fe_9S_{10}$ core for superior volumetric sodium/potassium storage, Energy Storage Mater. 24 (2020) 208–219.

[29] B.H. Hou, Y.Y. Wang, J.Z. Guo, Q.L. Ning, X.T. Xi, W.L. Pang, A.M. Cao, X. Wang, J.P. Zhang, X.L. Wu, Pseudocapacitance-boosted ultrafast Na storage in a pie-like FeS@ C nanohybrid as an advanced anode material for sodium-ion full batteries, Nanoscale 10 (2018) 9218–9225.

[30] Y. Zhang, P. Zhu, L. Huang, J. Xie, S. Zhang, G. Cao, X. Zhao, Few-layered $SnS_2$ on few-layered reduced graphene oxide as Na-ion battery anode with ultralong cycle life and superior rate capability, Adv. Funct. Mater. 25 (2015) 481–489.

[31] V. Etacheri, O. Haik, Y. Goffer, G. Roberts, I. Stefan, R. Fasching, D. Aurbach, Effect of fluoroethylene carbonate (FEC) on the performance and surface chemistry of Si-nanowire Li-ion battery anodes, Langmuir 28 (2012) 965–976.

[32] W. Li, M. Zhou, H. Li, K. Wang, S. Cheng, K. Jiang, A high performance sulfur-doped disordered carbon anode for sodium ion batteries, Energy Environ. Sci. 8 (2015) 2916–2921.

[33] F. Wan, H.Y. Lü, X.L. Wu, X. Yan, J.Z. Guo, J.P. Zhang, G. Wang, D.X. Han, L. Niu, Do the bridging oxygen bonds between active Sn nanodots and graphene improve the Li-storage properties? Energy Storage Mater. 5 (2016) 214–222.

[34] Y. Gao, Y.S. Xu, S.H. Xiang, X.Y. Zhang, Z.L. Li, H.J. Zhou, Nitrogen-doped carbon nanotube encapsulated $Fe_7S_8$ nanoparticles for the high-efficiency and selective removal of $Pb^{2+}$ by pseudocapacitive coupling, Environ. Sci.: Nano 9 (2022) 2051–2060.

[35] G. Wang, Y. Qi, D. Zhang, J. Bao, L. Xu, Y. Zhao, J. Qiu, S. Yuan, H. Li, Rational Design of Porous $TiO_2$@N-Doped Carbon for High Rate Lithium-Ion Batteries, Energy Technol. 7 (2019) 1800911.

[36] J. Wang, X. Yan, Z. Zhang, H. Ying, R. Guo, W. Yang, W.Q. Han, Facile preparation of high-content N-doped CNT microspheres for high-performance lithium storage, Adv. Funct. Mater. 29 (2019) 1904819.

[37] Z. Li, Y. Tan, N-doped mesoporous carbon/graphene aerogels as sulfur hosts for high-performance lithium-sulfur batteries, ChemistrySelect 3 (2018) 4319–4323.

[38] J. Luo, W. Hu, Z. Suo, Y. Wang, Y. Zhang, Co-pyrolysis of spent radioactive ion exchange resin and manganese dioxide: decrease the decomposition temperatures of functional groups, J. Hazard. Mater. 418 (2021) 126275.

[39] F. Xie, Z. Xu, A. Jensen, H. Au, Y. Lu, V. Araullo-Peters, A.J. Arew, Y.S. Hu, M.M. Titirici, Hard-Soft carbon composite anodes with synergistic sodium storage performance, Adv. Funct. Mater. 29 (2019) 1901072.

[40] D.A. Stevens, J.R. Dahn, An in situ small-angle x-ray scattering study of sodium insertion into a nanoporous carbon anode material within an operating electrochemical cell, J. Electrochem. Soc. 147 (2000) 4428–4431.

[41] M. Zheng, Y. Liu, Q. Ru, J. Zhang, Z. Pan, Y. Gao, F. Ling, L. Wei, Novel antimony phosphate loaded on grid-like N, S-doped carbon for facilitating sodium-ion storage, Chem. Eng. J. 415 (2021) 128942.

[42] B.Y. Chang, S.M. Park, Electrochemical impedance spectroscopy, Annu. Rev. Anal. Chem. 3 (2010) 207–229.

[43] K.J. Zhang, P.X. Hang, L. Gu, L.X. Zhang, Z.H. Liu, Q.S. Kong, C.J. Zhang, S.M. Dong, Z.Y. Zhang, J.H. Yao, H.X. Xu, G.L. Cui, L.Q. Chen, Synthesis of nitrogen-Doped MnO/Graphene nanosheets hybrid material for lithium ion batteries, ACS Appl. Mater. Interfaces 4 (2012) 658–664.

[44] Y. Zhang, X. Li, P. Dong, G. Wu, J. Xiao, X. Zeng, Y. Zhang, X. Sun, Honeycomb-like hard carbon derived from pine pollen as high-performance anode material for sodium-ion batteries, ACS Appl. Mater. Interfaces 10 (2018) 42796–42803.

[45] T. Yang, J. Zhong, J. Liu, Y. Yuan, D. Yang, Q. Mao, X. Li, Z. Guo, A general strategy for antimony-based alloy Nanocomposite embedded in Swiss-cheese-like nitrogen-doped porous carbon for energy storage, Adv. Funct. Mater. 31 (2021) 2009433.

[46] K. Wu, K. Du, G. Hu, A novel design concept for fabricating 3D graphene with the assistant of anti-solvent precipitated sulphates and its Li-ion storage properties, J. Mater. Chem. A 6 (2018) 3444–3453.